Acta Cryst. (1988). A44, 838-847

Structure Determination of Planar Defects in Crystals of Germanium and Molybdenum by HREM

BY A. BOURRET, J. L. ROUVIERE AND J. M. PENISSON

DRF, Service de Physique/Structure, CEN-Grenoble, 85X, 38041 Grenoble CEDEX, France

(*Received* 8 *January* 1988; *accepted* 18 *April* 1988)

Abstract

The possibility of the structure determination of planar defects in crystals by high-resolution electron microscopy (HREM) is presented. The optimum conditions for a direct visual interpretation of the projected structure are discussed using two typical examples: a $\Sigma = 5$ tilt grain boundary in germanium and a $\Sigma = 41$ grain boundary in molybdenum. It is shown that two particular defect images taken at the Scherzer defocus and at reverse contrast enable an approximate input structure to be found which can be employed to start a trial-and-error method. A practical procedure improving this input structure is proposed on the basis of the calculated positioning errors. It is demonstrated that positioning errors are mainly due to the electron microscope transfer function. The effect of crystal tilt is shown to modify greatly the atomic column visibility at the interface plane. Finally three-dimensional analysis of an interface is proposed by observation of it along two (or more) low-index axes. This procedure is illustrated on the Ge $\Sigma = 5$ grain boundary observed along [001] and [310].

1. Introduction

The mechanical, chemical and electronic properties induced in a number of polycrystalline materials by the presence of grain boundaries (GBs) as well as general interfaces critically depend on their atomic structures. In recent years, thanks to the availability of improved instruments, high-resolution electron microscopy (HREM) has provided qualitative information on atomic positions on or near a GB plane (Bourret & Bacmann, 1985; Krakow, Wetzel & Smith, 1986; Nowicki, Penisson & Biscondi, 1988). In most cases, a relatively direct interpretation of the projected structure is performed on experimental images from which several plausible atomic models are deduced. For instance, in semiconductor materials, a large amount of *a priori* information, such as the atomic radii or the coordination number fixed at four, is used to build a hypothetical stick and ball model (Bourret & Bacmann, 1987). In a few cases, computer-simulated images are calculated starting from these hypothetical structures or from available computer-relaxed structures. They are adjusted to the experimental images by a trial-and-error method (d'Anterroches & Bourret, 1984; Bourret, Billard & Petit, 1985; Nowicki, Penisson & Biscondi, 1988). From this tedious procedure, an accuracy of one-tenth of the resolution limit is obtained in positioning the atomic columns (Bourret, Thibault-Desseaux, d'Anterroches, Penisson & de Crecy, 1982). Until direct deconvolution algorithms are made useful in practice, it is necessary to improve the trial-and-error method.

This paper deals with the question of selecting optimum conditions for providing a reliable direct visual interpretation. It also suggests how to correct, if necessary, the projected atomic column location as deduced from the experimental images. A practical procedure to select the points at which such a correction is necessary is given. This provides a means of improving the 'input structure' selected for starting the trial-and-error method.

2. Relaxation at grain boundary interfaces

In principle, pure tilt GBs are ideal interfaces for testing the ability of HREM to perform a complete crystallographic analysis because the structure determination is supposed to be reduced to a two-dimensional case. This is, however, not the general case at more general interfaces or for more localized defects and it seems necessary to explore the possibility of obtaining three-dimensional arrangements. The use of two (or more) projections of the same interface could give information on the possible relaxation of atoms along one of the axes of observation. This possibility allows a more accurate selection of the initial input structure which can be exploited whenever possible. Two examples of GBs are studied in detail because they cover several typical situations which occur experimentally, namely the $(\bar{1}30)$ $\Sigma = 5$ in germanium with a [001] common axis, and the (910) $\Sigma = 41$ in molybdenum with a [001] common axis. In both cases, bicrystals are available and detailed experimental studies have already been performed with 400 kV high-resolution electron microscopes. For molybdenum, reported results (Penisson, Nowicki & Biscondi, 1988) have shown that the capped triangular prism model is very close to the

0108-7673/88/060838-10$03.00

one deduced from a direct interpretation. This model has no relaxation along the axis of observation and therefore does not require several projections. Experimental images have been obtained at −450 Å defocus, at which atomic columns appear black. In germanium, Papon, Petit, Silvestre & Bacmann (1983) have shown by electron diffraction that a very important relaxation occurs along the [001] common axis not only at the grain boundary plane but also for both crystals giving a large rigid-body translation along [001]. The proposed model is a reconstructed structure having a mirror glide symmetry [($\bar{1}30$) plane] and a 1/8 [001] rigid-body translation. This model is completely confirmed by HREM observations at 400 kV along two axes of observation [310] and [001] which are common to both crystals (Fig. 1). In both cases, focusing series are available with either black or white atomic columns.

In molybdenum, as well as in germanium, computer molecular static relaxation is available. An empirical interatomic potential of the Mie type has been used in the case of molybdenum $\Sigma = 41$ (Penisson *et al.*, 1988). The relaxed GB structure contains a capped triangular prism which forms the dislocation core structural unit. This unit when projected along the [001] axis forms a large hole (Fig. 2). For germanium, a modified Tersoff potential (Tersoff, 1986; Heggie & Jones 1987) is employed. The relaxed $\Sigma = 5$ GB structure contains in the [001] projection an array of pentagons and triangles assembled at a corner. The minimum energy is obtained for a rigid-body translation equal to 0·144[001], a value close to the one suggested by Papon *et al.* (1983). These projected relaxed structures show clearly that the distances between projected atomic columns are variable, very small in the triangles and large in the pentagons. Relaxed structures will be considered as the 'true input structures' in the rest of this paper.

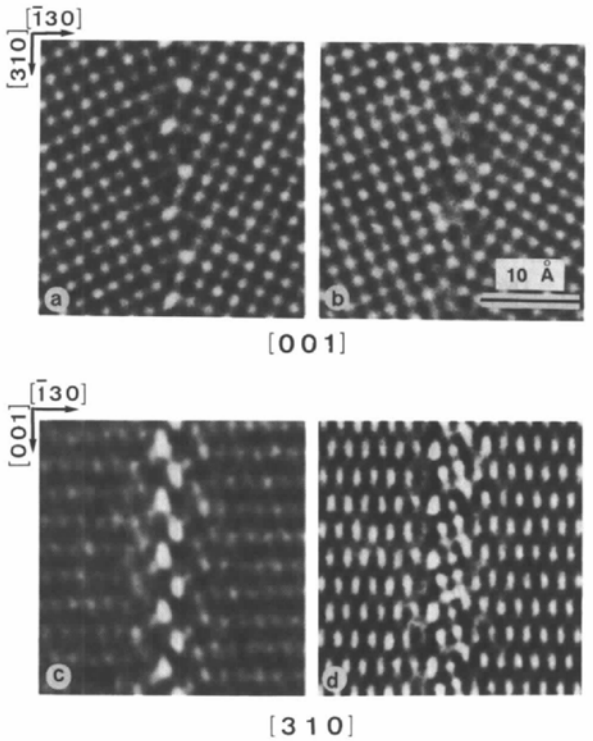

Fig. 1. Experimental images of a ($\bar{1}30$) $\Sigma = 5$ tilt grain boundary in germanium along two projection axes: [001] and [310]. The defocusing distances are about (*a*) −400 Å and (*b*) −700 Å along [001] and atomic columns are respectively black in (*a*) and white in (*b*) (reverse contrast). The defocusing distances are about (*c*) −500 Å and (*d*) −700 Å along [310] and atomic columns are respectively black in (*c*) and white in (*d*). Accelerating voltage 400 kV. $C_s = 1{\cdot}0$ mm.

3. Image simulation methods

Multislice image simulations (Cowley, 1981) were performed using software developed by Skarnulis (1982) and including absorption effects. Absorption is phenomenologically introduced by an imaginary potential based on the Radi (1970) calculation. The pixel number in direct space as well as in Fourier space is equal to 128 × 128. Slice thicknesses have been chosen equal to one period along the axis of observation *i.e.* 5·66 Å for Ge and 3·14 Å for Mo. However, for large periods and especially in the case of Ge $\Sigma = 5$ observed along [130], the period has been divided into five different slices. This slicing introduces upper-layer diffraction effects which could affect the dynamical propagation for large period (Lynch, 1971). However, in all the situations tested, these effects were found to be negligible.

Particular care has been taken in defining the window size ($A \times B$) in order to minimize the edge and spurious effects due to sampling. By using the periodic extension method, a large supercell of dimensions *A*, *B* is created. The GB plane is located on the symmetry plane parallel to *A*. The value of *A* is adjusted so that it contains an integer number (a power of two is preferable) of GB period (generally one or two).

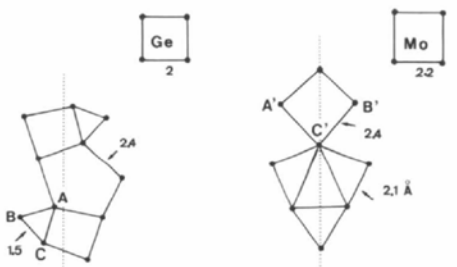

Fig. 2. Sketch of the tunnels formed in the [001] projection of grain boundaries in Ge $\Sigma = 5$ and Mo $\Sigma = 41$. These atomic positions are from computer-relaxed structures. Projected lengths (Å) are reported at important points. The scale is similar for both materials and only typical structural units of the GB plane are represented.

This period is equal to 8·95 Å for Ge $\Sigma = 5$ and 28 Å for Mo $\Sigma = 41$. In the B direction, the largest size compatible with a good spatial resolution is chosen. In practice, the sampling was 0·14 Å for Ge and 0·22 Å for Mo along the B axis. The exact atomic position column with respect to the sampling points is also important. It should be chosen so that it respects as much as possible the symmetry operations leaving the GB structure unchanged. For instance, the sampling errors should satisfy the presence of a mirror symmetry for Mo $\Sigma = 41$ and a mirror glide symmetry for Ge $\Sigma = 5$.

4. Image simulation of [001] tilt GB

4.1. *Optimum defocus and thickness*

The optimum defocus and thickness can be deduced from the inspection of the diffracted wave behaviour in a perfect crystal combined with the usual electron microscope transfer function.

In the case of a limited number of diffracted beams included in the objective aperture, the perfect-crystal contrast can be predicted by applying a pseudo-transfer function. This function can be written as (Desseaux, Renault & Bourret, 1977)

$$T(t, \Delta z) = \cos[\chi_g - \chi_0 - (2\pi/\lambda) \times (C_s g^4 \lambda^4/4 + \Delta z g^2 \lambda^2/2)] \qquad (1)$$

where $\chi_g - \chi_0$ is the dynamical phase shift between the 0 and g beams and is a function of thickness t, C_s is the spherical aberration coefficient, and Δz is the defocusing distance.

For [001] Ge as well as [001] Mo, four equivalent beams dominate the image formation (220 for Ge and 110 for Mo). Therefore the transfer function will be controlled by a single g modulus.

The multislice calculation on perfect [001] crystals in both materials gives the amplitudes and phases of the dominant beams. Fig. 3 shows the behaviour of 000, 220 and 400 beams as a function of the sample thickness in germanium while Fig. 4 shows the behaviour of 000, 110 and 200 beams in molybdenum.

Along the [001] zone axis in germanium, one extinction distance is clearly dominant for all beams and equal to $\xi = 260$ Å. However, in molybdenum, along the same [001] zone axis, two extinction distances are present with very different values, $\xi_1 = 55$ and $\xi_2 \sim 400$ Å (the latter is difficult to measure owing to absorption). This difference between the two materials is explained by the atomic densities in the ratio 5·65 : 3·14 along a column and the atomic number difference.

From Figs. 3 and 4 the optimum thickness is chosen with the following criteria: (i) the experimental signal-to-noise ratio should be large enough to eliminate thicknesses smaller than 50 Å; (ii) the contrast should be large enough; this is the case for the range 0·25 ξ_0–0·8 ξ_0 in germanium, and is satisfied for thicknesses larger than ξ_1 in molybdenum. In practice 0·4 ξ_0 and 0·8 ξ_0 are selected in germanium whereas ξ_1 and $2\xi_1$ are chosen in molybdenum.

Thus from (1) the transfer function of the dominant diffracted beams is calculated at 400 kV with C_s = 1·0 mm. The contrast plot of T as a function of defocus, Δz, and thickness, t, is then deduced (Figs. 5 and 6). These figures enable the determination of the experimental parameters which give maximum positive ($T = +1$, atoms are white) as well as maximum negative contrast ($T = -1$, atoms are black). The case $T = 0$ corresponds to the extinction of the fundamental frequencies in the image. Double periodicities are then observed (Desseaux *et al.*, 1977). In practice, however, the simple formula (1) should be modified in order to take into account the

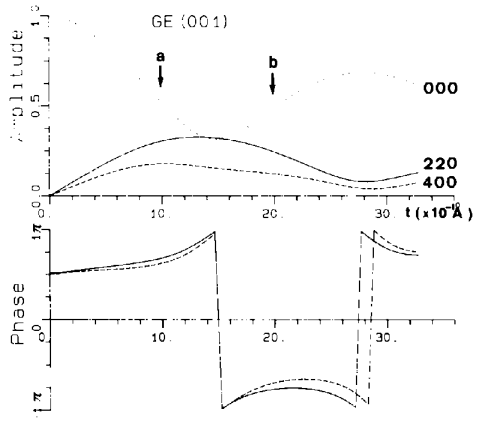

Fig. 3. Dynamical phases and amplitudes of the three main beams diffracted by a [001] germanium crystal as a function of thickness t. Phases are relative to the 000 beam. The points a and b are the selected thicknesses for simulating GB images.

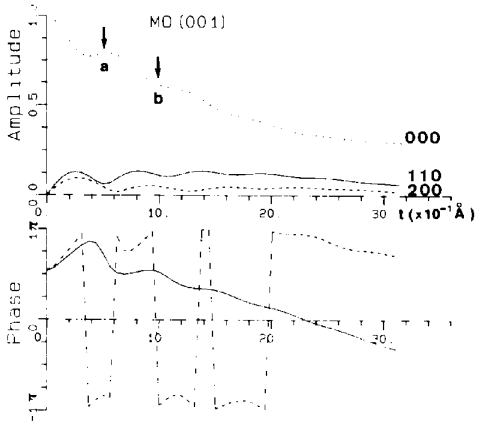

Fig. 4. Dynamical phases and amplitudes of the three main beams diffracted by a [001] molybdenum crystal as a function of thickness t. Phases are relative to the 000 beam. The points a and b are the selected thicknesses for simulating GB images.

beam divergence. This effect is minimized when using the stationary conditions obtained at (or close to) a defocus (Spence, 1981),

$$\Delta z_s = -C_s g^2 \lambda^2. \quad (2)$$

This defocus is equal to −680 and −560 Å in germanium and molybdenum respectively. Consequently, only three selected defocusing distances are useful in practice: the first is close to the Scherzer distance and the atomic columns are black, the second is very close to the stationary condition (2) and the atomic columns are white, the third, for still higher negative defocus value, is also with black atoms. It is worthwhile to note that the selected defoci giving high contrast ($T = 1$ or -1) are thickness dependent.

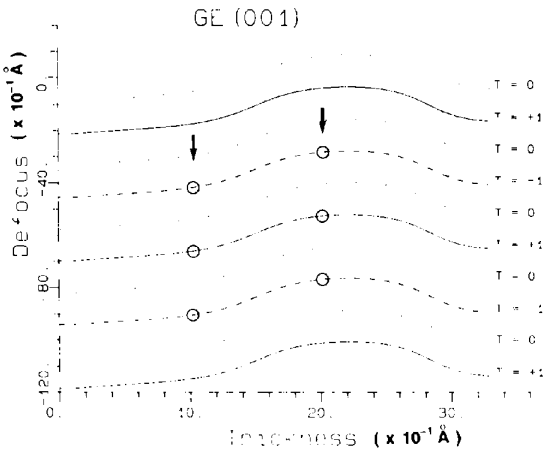

Fig. 5. Maximum positive ($T = +1$) or negative ($T = -1$) contrast of the 220 beams in [001] germanium as a function of defocus and foil thickness. Points employed for image simulation are marked by a circle. Atomic columns appear black at $T = -1$ and white at $T = +1$.

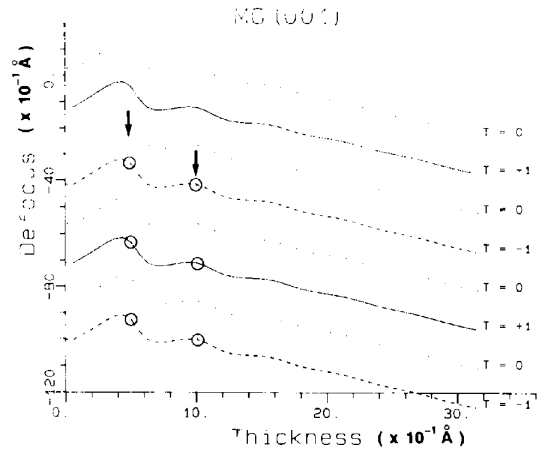

Fig. 6. Maximum positive ($T = +1$) or negative ($T = -1$) contrast of the 110 beams in [001] molybdenum as a function of defocus and foil thickness. Points employed for image simulation are marked by a circle. Atomic columns appear black at $T = -1$ and white at $T = +1$.

Table 1. *Selected conditions for obtaining high-contrast HREM images in perfect* [001] Ge *and* Mo; *accelerating voltage* = 400 kV, $C_s = 1$ mm

	Thickness t (Å)	Defocus Δz (Å) First band	Second band	Third band
Ge	102	−420	−660	−900
[001]	215	−280	−525	−760
Mo	50	−350	−650	−850
[001]	100	−420	−720	−1020
Atomic column contrast		Black	White	Black

For instance, the appropriate defocus with $T = -1$ at $0{\cdot}4\xi_0$ gives $T = 0$ at $0{\cdot}8\xi_0$. The experimental conditions are always selected by the operator at a maximum contrast in one of the previously determined conditions as summarized in Table 1.

4.2. *Validity of direct visual interpretation of the projected structure*

In perfect crystals, the selected optimum conditions give images which are directly interpretable. The [001] HREM images are formed from squares which represent the projected structure of the perfect crystals. The atomic column positions can be accurately deduced provided the two experimental parameters t and Δz are known, at least approximately. In defect crystals, as in the GB plane, this simple situation is no longer valid and requires more detailed image simulation.

Images of relaxed Ge $\Sigma = 5$ and Mo $\Sigma = 41$ structures were computer simulated using the conditions given in Table 1. The following parameters were employed: accelerating voltage 400 kV, spherical aberration $C_s = 1$ mm, beam divergence = 0·7 mrad and energy spread = 70 Å.

Fig. 7 shows that imaging Ge $\Sigma = 5$ using the first defocus band produces white dots in tunnels. The three tunnel types, squares, triangles and pentagons, are easily distinguished. The pentagonal tunnel gives a large elongated white dot. The small triangular tunnel, on the other hand, is hardly visible, especially for small thicknesses. For the second defocus band, all atomic columns are well imaged except for atoms forming the triangle. For the third defocus band, several artefacts are visible. The large pentagonal tunnel either disappears or is marked by two distinct white points. Equally, the triangular tunnel is hardly visible.

In Mo $\Sigma = 41$ (Fig. 8) imaging with the first or second defocus band is excellent and a direct visual interpretation of the structure is possible. All the tunnel types are well imaged and atomic columns are clearly visible. Positioning errors are limited to the three atoms A', B' and C' (see Fig. 2). In the second defocus band, the positioning error is limited to 0·28 Å for atom C' and 0·25 Å for atom A' or B'. In

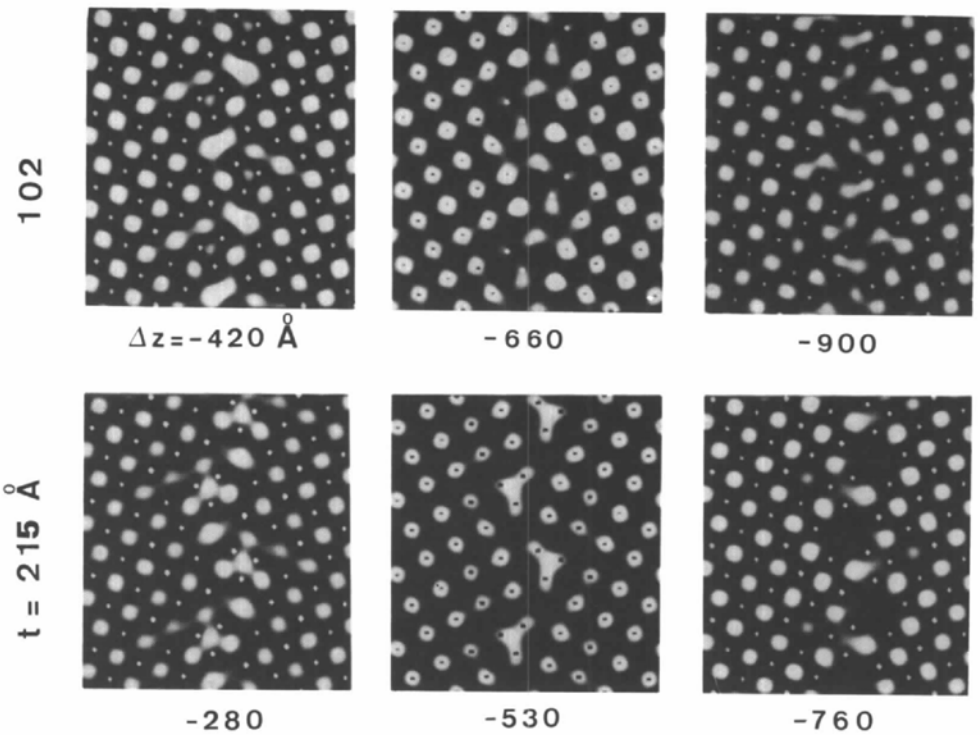

Fig. 7. Simulated images of Ge $\Sigma = 5$ at different defoci for two foil thicknesses, $t = 102$ and 215 Å. Accelerating voltage 400 kV, $C_s = 1{\cdot}0$ mm. Projected atomic positions are marked with black or white points.

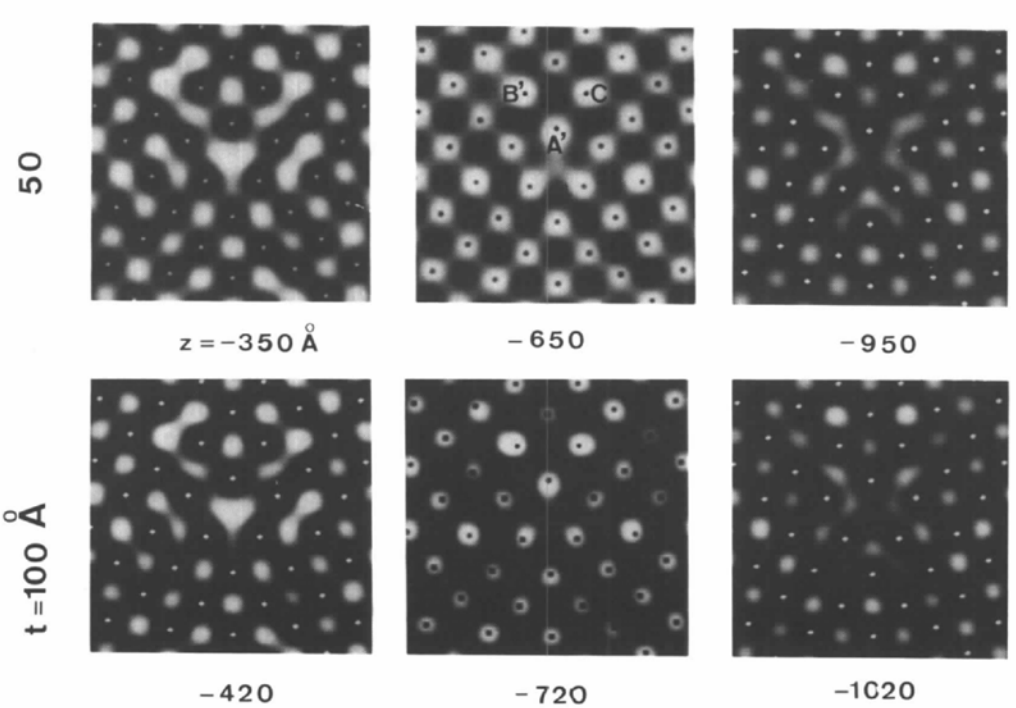

Fig. 8. Simulated images of Mo $\Sigma = 41$ at different defoci for two foil thicknesses, $t = 50$ and 100 Å. Accelerating voltage 400 kV, $C_s = 1{\cdot}0$ mm. Projected atomic positions are marked with black or white points.

the third defocus band, artefacts appear in the large tunnel in the form of two well separated white dots.

Errors in directly locating the atomic column positions at maximum (or minimum) intensity points have been quantitatively measured in Ge $\Sigma = 5$. An enlarged portion of the grain boundary plane (Fig. 9) at pentagonal and triangular structural units enables the measurement of the displacement vector **x** joining the initial atomic column projection to the maximum (white atoms) or minimum (black atoms) intensity. In the latter case, however, a subsidiary maximum is sometimes present owing to the presence of half periodicities which prevent an automatic search with the usual image processing software function. A direct measurement on printed images is performed in this case. Table 2 summarizes the displacement-vector amplitudes or positioning error made from a direct visual interpretation of the structure. It shows that positioning errors are large in the second band defocus and even more in the third band. By contrast, they remain smaller than 0·42 Å in the first band close to the Scherzer defocus. The accuracy in the determination of the positioning errors is of the order of half the sampling distance.

In order to understand the origin of these positioning errors, one has to distinguish between two effects (Tanaka & Cowley, 1987). The first is due to the dynamical interaction in the crystal itself and the second is due to the electron microscope aberrations. The effect of dynamical interaction is obtained by calculating the aberration-free image ($C_s = 0$) at a defocus which restores large maximum intensity (or minimum) at atomic column sites. The exit face of the foil is generally not suitable for this purpose as a result of the oscillating nature of the wave function between atomic columns in the crystal. A defocus equal respectively to −90 and +80 Å at a 102 and 215 Å thick crystal gives a minimum intensity at the exact atomic column position. The resulting aberration-free images are reported in Fig. 10 for a limiting objective aperture of 0·714 $Å^{-1}$. They show that small positioning errors are already detectable. The triangular tunnel is hardly visible at small thicknesses and it is not exactly centred. In the same manner, the atoms *A* and *C* are not exactly centred in the black squares demarcated by the white walls. This error increases slightly with thickness (see Table 2). Meanwhile the intensity distribution in the pentagonal and triangular tunnels is very much affected.

Table 2. *Positioning errors induced by a direct read-out of a* Ge $\Sigma = 5$ *grain boundary image*

These errors are calculated by measuring the distance between the true atomic position and the closest extremum of the calculated intensity distribution. All errors are given in 10^{-1} Å. *A*, *B* and *C* atoms refer to Fig. 2.

	A		*B*		*C*	
Thickness (Å)	102	215	102	215	102	215
Defocus						
first band	2·6	3·6	3·4	2·2	2·8	4·2
second band	6·1	2·6	2·6	6·8	5·6	≤1·5
third band	2·6	6·6	2·6	3·4	7·3	4·2
Aberration free	≤1	1·1	≤1	1·1	1·4	1·4

As shown by Van Dyck, Van Tendeloo & Amelinckx (1982) and Coene, Van Dyck, Van Tendeloo & Van Landuyt (1985) the lateral spread of the electron scattering at an end-on planar defect is limited to the Takagi triangle rather than to a column. Taking this criterion as the limit of determining strong interaction between columns, one is able to deduce the maximum thickness t_{max} at which such an interaction is important. If one sets the aperture at a value corresponding to the electron microscope information limit d_{min}, the Takagi condition is given by

$$t_{max} = (a_c/2\lambda)d_{min} \qquad (3)$$

where a_c is the distance between two nearest-neighbour projected atomic columns. Values of t_{max} are listed in Table 3 for 400 kV electrons.

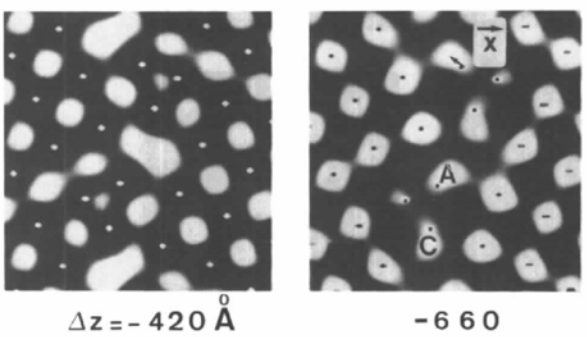

Fig. 9. Enlarged view of simulated images at the triangular and pentagonal tunnels in a Ge $\Sigma = 5$ grain boundary. Note the large displacement of the white dot at *A* and *C* atoms at −660 Å defocusing distance. Thickness 102 Å. The projected atomic column positions are indicated with black (or white) markers. From such images the positioning error vectors **x** can be determined.

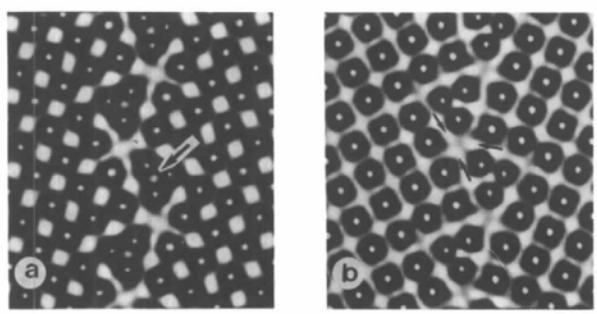

Fig. 10. Aberration-free images at (*a*) $t = 102$ Å, defocus −90 Å and (*b*) $t = 215$ Å, defocus +80 Å, for a Ge $\Sigma = 5$ grain boundary. White markers are the projected atomic column positions. Limiting aperture $R = 0{\cdot}714$ $Å^{-1}$. Note the very low intensity in the triangular tunnel in (*a*), and the three subsidiary maxima appearing in the pentagonal tunnel in (*b*).

Table 3. *Maximum thickness determined by the Takagi condition for having independent atomic columns as a function of the projected distance, a_c, between them*

The information limit (and the aperture function) is equal to 1·3 Å for 400 kV electrons.

a_c (Å)	1·5	1·7	2	2·5
t_{max} (Å)	59	67	78·8	98·5

Values listed in Table 3 indicate that in Mo $\Sigma = 41$, atomic columns act quite independently even in 100 Å thick foil (see Fig. 2 for distances between columns). This is not the case in Ge $\Sigma = 5$, in which interaction between atomic columns *A* and *B* occurs even in the thinner case. This dynamical effect is enhanced by the transfer function distortion which increases when atomic distances are smaller. This explains why positioning errors are smaller in molybdenum for which both effects are minimized due to larger average distances between atomic columns.

Several important consequences can be deduced from the above analysis: (i) Positioning errors occur precisely at the atomic columns which form the most interesting part of the GB structure. (ii) The best projected structure has to be deduced from the first defocus band. However, some tunnels may be hardly visible if they are too small and the exact number of atomic columns is not very easy to assess at this defocus. Therefore one has to use the second band at which all the atomic columns are visible to determine the first input structure. A more precise positioning can then be performed on the first defocus band image. (iii) A quantitative comparison between the two inverse contrast images (first and second band) is then necessary. At all points at which complementary intensities are not observed, the positioning error is likely to be large. This fact is clearly shown in Table 2 where positioning errors in the two different defoci are always different. Therefore a practical procedure is suggested which consists of adding the first- and second-band experimental images to detect the points at which corrections should be applied. The atomic columns which form the first input structure are then moved in a direction given by the intensity gradient of the added image (from a maximum to a minimum of the average intensity). The exact amplitude of the correction cannot be predetermined and is finally adjusted by a trial-and-error method. The advantage of this practical procedure is to minimize the number of parameters by selecting the atomic column positions which should be corrected and giving the error vector direction. (iv) Positioning errors are mainly due to the transfer function distortion. Therefore it should be sufficient to restore an 'aberration-free' image limited to the information resolution to correct the major part of the positioning error due to a direct interpretation. Several algorithms have been proposed for this purpose among which the one sug-

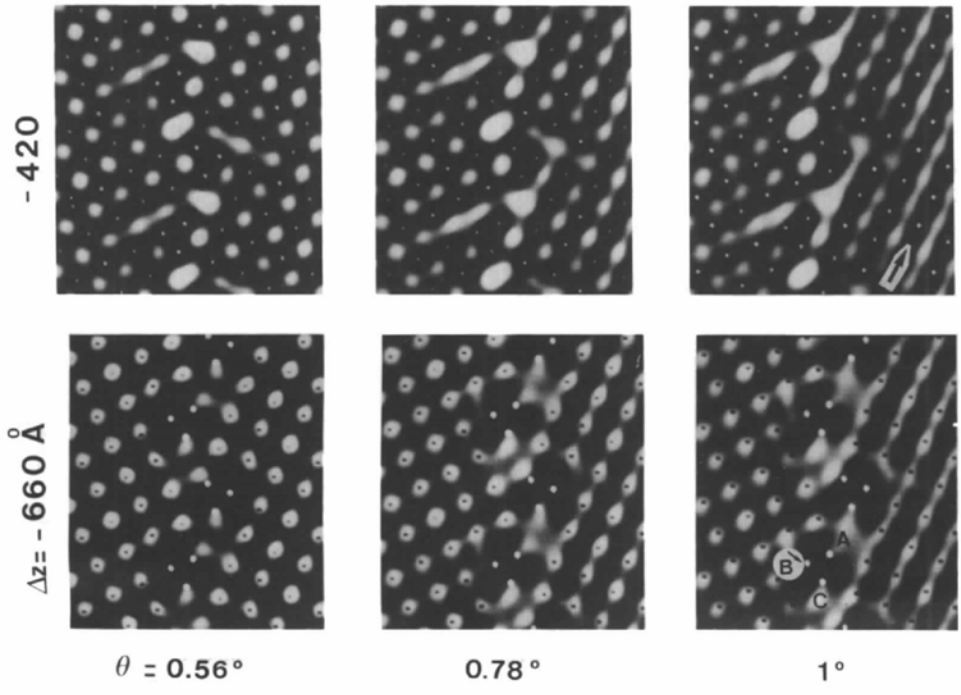

Fig. 11. Effect of crystal tilt on the Ge $\Sigma = 5$ grain boundary image. The crystal tilt is performed in an oblique direction with respect to the GB plane (indicated by an arrow). Thickness 100 Å, 400 kV, $C_s = 1{\cdot}0$ mm. Two defocusing distances give reverse contrast: first band at −420 Å and second band at −660 Å.

gested by Van Dyck & Coene (1987) is particularly attractive. In this context, the difficult task of retrieving by a recursive scheme the projected potential is not urgently needed.

4.3. *Influence of crystal tilt on the direct visual interpretation*

Once the microscope is correctly aligned by the usual procedure, the only remaining experimental error is a crystal tilt or a misalignment of the atomic columns along the optical axis. The accuracy in the goniometer stages and specimen buckling often introduce errors of the order of 0·5 to 1°. Although such a crystal tilt is easily detected on thick specimens *via* the Kikuchi lines, in thin regions the diffraction pattern is less sensitive to small tilt angle.

In order to study the effect of a mistilt by an angle θ on the atomic column positioning, a series of simulated images of the tilted Ge $\Sigma = 5$ structure are calculated (Fig. 11). The tilt direction is selected along a ⟨110⟩ direction of one grain (inclined at 26·6° from the GB plane). This direction destroys the initial symmetries. The strongest effect at small tilt angle is the disappearance of the triangular tunnel in the first band and the disappearance of the atomic column *B* in the second band. It should be noted that this effect is present although both crystals seem to be correctly imaged and elongated spots are hardly visible ($\theta =$ 0·56°). In addition, the symmetry elements are not visibly changed at small mistilt values and the mirror glide symmetry along the GB plane is only weakly affected at $\theta \leq 0{\cdot}56°$. Moreover, the rigid-body translation is not perturbed by a mistilt even for values as large as $\theta = 0{\cdot}78°$ at which elongated spots are clearly visible. At $\theta = 1°$ the symmetry elements are no longer detectable but the rigid-body translation is still measurable without error, provided the atom contrast is known ($T = +1$ or -1).

The positioning errors for the three atomic columns *A*, *B* and *C* are given in Table 4 at the second band defocus. (The third band defocus is useless, being seriously deformed.)

The reference points which are to be used to measure the positioning errors are somehow arbitrary. They are chosen to be the projected atomic positions in the middle of the foil. With such markers the final image effectively corresponds to the projected atomic structure for small tilt angle. However, for large angles ($\theta = 1°$) an additional translation needs to be introduced. The projection corresponds to atomic positions closer to the foil exit face.

Table 4 shows, as expected, that positioning errors increase with the tilt angle. For misalignment $\theta \sim 0{\cdot}6°$, errors are doubled compared with $\theta = 0$, although the perfect crystal images are hardly affected. The only sign of mistilt is given by a slight difference in the spot shapes.

Table 4. *Positioning errors induced by a direct visual interpretation of the intensity extrema for a tilted* Ge $\Sigma = 5$ *GB image*

The tilt direction is indicated in Fig. 11. Second defocus band at −660 Å; thickness: 102 Å. The half projected lengths of an atomic column are also given as a reference. All distances are given in 10^{-1} Å. *A*, *B* and *C* atoms refer to Fig. 2.

Tilt angle (θ°)	0	0·56	0·78	1
Atom name				
A	6·1	7·8	8·4	Not visible
B	2·6	5·5 (very weak)	7·7 (weak)	10 (weak)
C	5·6	5·5	8·5	11
Half projected length	0	4·98	6·94	8·9

The right order of magnitude for mistilt can be obtained on a wedge crystal once the thickness is known. The size of the tunnels measured in the first defocus band is approximately given by the geometrical projection, *i.e.* $t \tan\theta$. Hence, after measurement in the thicker part of the specimen, the tilt angle can be employed in simulating images at the thinner part at which the mistilt is not directly visible. The most striking feature is visible in Fig. 11. One can see the almost complete disappearance of one atomic column (*B*) in the second-band image but with no corresponding white dot in the first band. This change intensifies the non-complementarity of reverse-contrast images (first and second band) and helps in determining the positions at which atomic columns have to be added or displaced (see above for the practical procedure). The main problem is then to find on experimental images the exact position at which superposition of the two images should be performed. In the GB, this choice is generally unambiguous, at least when the coincident site lattice is large.

5. Three-dimensional analysis of an interface

Once the procedure previously described is carried out on one interface projection, one has to repeat the same procedure on different projections in order to solve completely an interface structure. This task is even more complicated than before because several low-index zone axes are not always available. Such an approach was initiated on a {112} $\Sigma = 3$ grain boundary (Bourret *et al.*, 1985) but the information extracted from the second axis of observation was limited to overall parameters, rigid-body translation measurement and periodicity determination at the GB plane.

The Ge $\Sigma = 5$ may be observed along the [310] axis perpendicular to the first [001] axis of observation. Along this direction, atom pairs, 1·4 Å apart, can be distinguished (Bourret & Penisson, 1987). The projected structure is shown in Fig. 12 and compared with the [001] projection. The rigid-body translation along

[001] is clearly visible as observed experimentally (Fig. 1). In addition, very large displacements of individual atomic columns along the [001] axis are predicted, although the GB is of a pure tilt case. For instance, atom A relaxes by more than 0·6 Å and atom C by the same amount in the opposite direction. This relaxation opens up large tunnels in the projected structure along [310]. The simulated images (Fig. 13) at different defoci show that, once again, the first band (tunnel imaging) and the second band (atom imaging) are the most useful in finding the atom positions. It should be pointed out that not every atomic column is resolved. For instance, atoms C and D are not distinguishable in the second band. However, when solving the structure one has to take into account the fact that the same number of atoms in a given periodic volume are present in [001] and [310] projections. Moreover, two of the atom coordinates are already available from the structure determination of one projection. At higher defocusing distances, imaging of the perfect crystal is improved but the number of artefacts in the GB plane increases and a direct visual interpretation is no longer possible. Therefore these simulations suggest, once again, limitation of the observations to the first and second defocus band if one wants to build the input structure for the trial-and-error method. This will not be the case if restoration algorithms have to be applied. In this case higher defocusing distances with improved resolution could be useful.

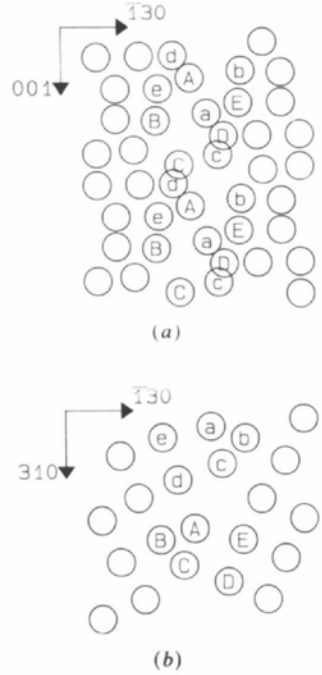

Fig. 12. Two atomic projections of Ge $\Sigma = 5$ along (*a*) [310] and (*b*) [001] axes. These positions are computer-relaxed structures using a modified Tersoff potential.

6. Concluding remarks

Among the two planar structures (Mo $\Sigma = 41$ and Ge $\Sigma = 5$) which are selected as typical examples of interfaces, the molybdenum GB is the easier to study. The [001] projection can be visually interpreted directly from an image taken close to the Scherzer defocusing distance (white tunnels) and the positioning error is limited to few atoms close to the capped triangular prism and is of the order of 0·25 Å. The direct 'read-out' structure can be employed as the input structure to start the trial-and-error method in computer simulation. Moreover, this GB is a typical example of an interface for which only one simple projection is sufficient.

In Ge $\Sigma = 5$, distances between several nearest-neighbour atomic columns are smaller than the Scherzer resolution limit of the 400 kV electron microscope. As a result, large positioning errors are observed on simulated images, particularly in the second or third defocus band (up to 0·7 Å). These errors are mainly due to the electron microscope transfer function and not to the dynamical interaction in the defect crystal. From the observation of two inverse contrast images, a practical way of improving the input structure determination can be deduced. It is important to have at

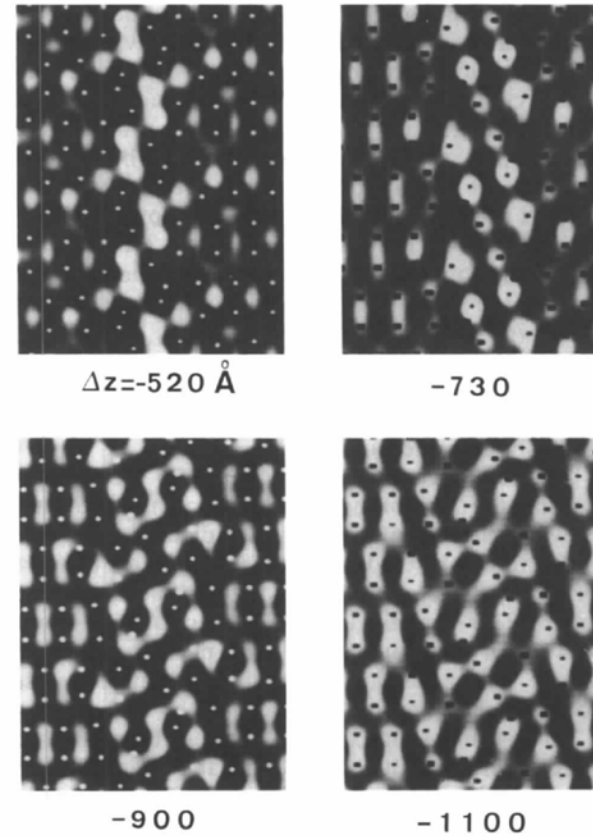

Fig. 13. Simulated images of Ge $\Sigma = 5$ along the [310] axis. Focusing series for a thickness of 107 Å, 400 kV, $C_s = 1{\cdot}0$ mm.

least two images in the first and second defocus bands in order to detect the points at which they are not complementary. The addition of these two images will give the direction in which the atomic columns should be moved in order to improve the accuracy of the input structure. Obviously, these conclusions are still valid for more general structures and planar interfaces. The important parameters are the distances between projected atomic columns. In all cases for which these distances are smaller than the Scherzer resolution limit the effect of the transfer function will result in a large distortion of the image. The determination of the selected defoci for imaging tunnels or atoms has to be studied in a specific case prior to the interface structure determination. It should, however, be concluded that there is an urgent need for developing a practical algorithm allowing deconvolution of the effect of the transfer function and restoration of an aberration-free image with a resolution limit close to the information limit.

References

ANTERROCHES, C. D' & BOURRET, A. (1984). *Philos. Mag. A*, **49**, 783-807.

BOURRET, A. & BACMANN, J. J. (1985). *Surf. Sci.* **162**, 495-509.

BOURRET, A. & BACMANN, J. J. (1987). *Rev. Phys. Appl.* **22**, 563-568.

BOURRET, A., BILLARD, L. & PETIT, M. (1985). *Inst. Phys. Conf. Ser.* **76**, 23-28.

BOURRET, A. & PENISSON, J. M. (1987). *JEOL News*, **25E**, 2-7.

BOURRET, A., THIBAULT-DESSEAUX, J., D'ANTERROCHES, C., PENISSON, J. M. & DE CRECY, A. (1982). *J. Microsc. (Oxford)*, **129**, 337-345.

COENE, W., VAN DYCK, D., VAN TENDELOO, G. & VAN LANDUYT, J. (1985). *Philos. Mag. A*, **52**, 127-143.

COWLEY, J. M. (1981). *Diffraction Physics*, 2nd ed. Amsterdam: North-Holland.

DESSEAUX, J., RENAULT, A. & BOURRET, A. (1977). *Philos. Mag.* **35**, 357-372.

HEGGIE, H. & JONES R. (1987). *Inst. Phys. Conf. Ser.* **87**, 367-374.

KRAKOW, W., WETZEL, J. T. & SMITH, D. A. (1986). *Philos. Mag. A*, **53**, 739.

LYNCH, D. F. (1971). *Acta Cryst.* A**27**, 399-407.

NOWICKI, T. N., PENISSON, J. M. & BISCONDI, M. (1988). Proc. Conf. Interface Science and Engineering, Lake Placid, New York, 1987. To be published in *J. Phys. (Paris)*.

PAPON, A. M., PETIT, M., SILVESTRE, G. & BACMANN, J. J. (1983). *J. Microsc. Spectrosc. Electron.* **8**, 135-146.

PENISSON, J. M., NOWICKI, T. & BISCONDI, M. (1988). Submitted to *Philos. Mag.*

RADI, G. (1970). *Acta Cryst.* A**26**, 41-56.

SKARNULIS, A. J. (1982) *J. Microsc. (Oxford)*, **127**, 39-46.

SPENCE, J. C. H. (1981). *Experimental High Resolution Electron Microscopy*. Oxford: Clarendon Press.

TANAKA, N. & COWLEY, J. M. (1987). *Acta Cryst.* A**43**, 337-346.

TERSOFF, J. (1986). *Phys. Rev. Lett.* **56**, 632-635.

VAN DYCK, D. & COENE, W. (1987). *Acta Cryst.* A**43**, C248.

VAN DYCK, D., VAN TENDELOO, G. & AMELINCKX, S. (1982). *Ultramicroscopy*, **10**, 263-280.

Acta Cryst. (1988). A**44**, 847-853

Electron Microscopy of Crystals with Time-Dependent Perturbations

BY J. M. COWLEY

Department of Physics, Arizona State University, Tempe, Arizona 85287-1504, *USA*

(*Received* 15 *February* 1988; *accepted* 20 *April* 1988)

Abstract

The electron microscope image intensity of a thin crystal is described as a time average of the image of a crystal perturbed by time-dependent fluctuations corresponding to thermal motion of the atoms or low-energy electronic excitations. For very thin crystals the phase-object approximation indicates that images having atomic resolution may be obtained from the inelastically scattered electrons. It is shown that the use of suitable approximations allows estimates to be made of the contribution of the inelastically scattered electrons to the high-resolution images of thicker crystals. The resolution of images formed by inelastically scattered electrons is not affected by the non-localization of the inelastic scattering process.

1. Introduction

Recent trends towards the more quantitative uses of electron microscopy have emphasized the need for a more complete assessment of the formation of images by the electrons inelastically scattered from the specimen (Cowley & Smith, 1987). Existing treatments such as those of Misell & Atkins (1973) and Kohl & Rose (1985) appear adequate for most moderate-resolution imaging but some uncertainties exist regarding the possibility that inelastically scattered electrons may contribute to the atomic-scale detail of high-resolution images of crystals.

For the scattering by phonons, or the thermal motions of atoms, it is usually considered adequate to apply a Debye-Waller factor to the atomic scattering amplitudes so that the potential distribution in

0108-7673/88/060847-07$03.00